

Article

Introducing Oxygen Vacancies in $\text{Li}_4\text{Ti}_5\text{O}_{12}$ via Hydrogen Reduction for High-Power Lithium-Ion Batteries

Yiguang Zhou, Shuhao Xiao, Zhenzhe Li, Xinyan Li, Jintao Liu, Rui Wu * and Junsong Chen * 

School of Materials and Energy, University of Electronic Science and Technology of China, Chengdu 610054, China; 202021030225@std.uestc.edu.cn (Y.Z.); 18653460879@163.com (S.X.); uestclizhenzhe@163.com (Z.L.); 18896552001@163.com (X.L.); liujt1989@163.com (J.L.)

* Correspondence: ruiwu0904@uestc.edu.cn (R.W.); jschen@uestc.edu.cn (J.C.)

Abstract: $\text{Li}_4\text{Ti}_5\text{O}_{12}$ (LTO), known as a zero-strain material, is widely studied as the anode material for lithium-ion batteries owing to its high safety and long cycling stability. However, its low electronic conductivity and Li diffusion coefficient significantly deteriorate its high-rate performance. In this work, we proposed a facile approach to introduce oxygen vacancies into the commercialized LTO via thermal treatment under Ar/H_2 (5%). The oxygen vacancy-containing LTO demonstrates much better performance than the sample before H_2 treatment, especially at high current rates. Density functional theory calculation results suggest that increasing oxygen vacancy concentration could enhance the electronic conductivity and lower the diffusion barrier of Li^+ , giving rise to a fast electrochemical kinetic process and thus improved high-rate performance.

Keywords: $\text{Li}_4\text{Ti}_5\text{O}_{12}$; oxygen vacancy; high-rate performance; electronic conductivity; density functional theory



Citation: Zhou, Y.; Xiao, S.; Li, Z.; Li, X.; Liu, J.; Wu, R.; Chen, J. Introducing Oxygen Vacancies in $\text{Li}_4\text{Ti}_5\text{O}_{12}$ via Hydrogen Reduction for High-Power Lithium-Ion Batteries. *Processes* **2021**, *9*, 1655. <https://doi.org/10.3390/pr9091655>

Academic Editor: Sergey Zhironkin

Received: 21 July 2021

Accepted: 8 September 2021

Published: 14 September 2021

Publisher's Note: MDPI stays neutral with regard to jurisdictional claims in published maps and institutional affiliations.



Copyright: © 2021 by the authors. Licensee MDPI, Basel, Switzerland. This article is an open access article distributed under the terms and conditions of the Creative Commons Attribution (CC BY) license (<https://creativecommons.org/licenses/by/4.0/>).

1. Introduction

Lithium-ion batteries (LIBs), as the dominant energy storage device, have been widely applied in portable electronic devices and electric vehicles [1–4]. Even though graphite could be considered as the most successful anode material for LIBs [5–7], it still suffers from large volume expansion, poor rate capability arising from its low Li^+ diffusion coefficient, and also dendrite formation which would cause severe safety problems [8,9]. As a result, graphite may not be suitable for applications where safety and low-frequency maintenance are the primary concerns, such as batteries for buses or large-scale power plants.

Recently, spinel $\text{Li}_4\text{Ti}_5\text{O}_{12}$ (LTO) has attracted a lot of attention as a deintercalation/intercalation anode material due to its high safety and long cycling stability, which is associated with its negligible volume variation (also known as “zero strain”) during the Li^+ insertion/extraction process through the three-dimensional diffusion channels [10–12]. Meanwhile, LTO possesses a high operation voltage (1.55 V vs. Li/Li^+) that can, to some extent, avoid the formation of the solid electrolyte interphase (SEI) and Li dendrites. However, the intrinsically low electronic conductivity ($10^{-13} \text{ S cm}^{-1}$) and limited lithium diffusion coefficient (10^{-9} – $10^{-13} \text{ cm}^2 \text{ s}^{-1}$) [13–15] of LTO, originating from the absence of electrons in the Ti 3d orbitals, leads to its large band gap (2 eV), thus preventing its more intensive applications.

To address these drawbacks, metal atom doping could be quite effective, such as Cr, Na, Gd and W, which would have a positive impact on the structure and stability of LTO during lithium intercalation and de-intercalation [16–19]. On the other hand, several works have indicated that the electrochemical properties of LTO could also be improved by the introduction of oxygen vacancies (OVs), which can narrow the band gap by creating defects, thus enhancing the electrical conductivity of different materials [20–24] such as TiO_2 , Co_3O_4 and LTO. The OVs are usually generated by treating the materials under reducing atmosphere (i.e., H_2), argon or vacuum [25], reacting with metal or hydride, hydrothermal

reactions and plasma treatments [24,26]. Even though it has been demonstrated that plasma treatments under reducing atmospheres could be efficient in generating OVs in LTOs which led to the reduction of Ti^{4+} to Ti^{3+} while at the same time enhancing lithium storage performance [20,21,24], this method might not be commercially feasible at a large scale due to its high cost and complicated operation process.

Herein, we facilely treated commercialized LTO under a reduced atmosphere of Ar/H_2 (5%) for the successful generation of OVs in LTO. As demonstrated by density functional theory calculations, the increasing concentration of OVs could lead to a tuned electronic structure and a low interaction of Li^+ and LTO surface. As a result, the H_2 -treated LTO demonstrated much better high-rate performance and long-term cycling stability than the untreated pristine LTO. Both the theoretical and experimental analysis confirmed that the current H_2 treatment was highly efficient and cost-effective in introducing OVs into LTO, leading to greatly enhanced lithium storage properties, thus demonstrating great potential for large-scale high-power applications.

2. Materials and Methods

2.1. Modification of LTO

0.5 g commercial LTO (Tianjiao Technology Development Co., Kuiyong Town, China) was put into a porcelain boat with a size of 60 cm in length and 30 cm in width and treated in a tube furnace (OTF-1200X) by annealing under Ar/H_2 (5%) atmosphere and the size of tube was 8 cm in diameter and 1 m in length. In particular, the rate of heat rate was $2\text{ }^\circ\text{C min}^{-1}$ with a 50 mL min^{-1} of gas flow rate and the temperature of $450\text{ }^\circ\text{C}$ for 1 h.

2.2. Material Characterization

The crystallographic phases of all samples were investigated by X-ray diffraction (XRD Bruker, D8 Advancer; Using $\text{Cu K}\alpha$ radiation in the range of $2\theta = 10\text{--}80^\circ$ with $50\text{ kV } 30\text{ mA}$, $\lambda = 1.54\text{ \AA}$). The morphologies of HLTO and LTO were characterized via transmission electron microscope (TEM; JEM2010F; FEI Talos-s, 200 kV accelerator voltage), selected area electron diffraction (SAED) and field emission scanning electron microscope (FSEM; FEI Inspect F50, Thermo Fisher Scientific, Waltham, MA, USA). X-ray photoelectron spectroscopy (XPS, Thermo Fisher Scientific Escalab 250Xi; $\text{Al K}\alpha$ $h\nu = 1486.6\text{ eV}$; working voltage 12 kV and filament current 6 mA, Thermo Fisher Scientific, Waltham, MA, USA) measurements were carried out to determine the chemical state of samples. Raman spectroscopy tests were performed on a Thermo Fisher Scientific DXR Raman spectrometer with an excitation wavelength of 532 nm. The specific surface area of LTO and HLTO was acquired by N_2 adsorption–desorption Brunauer–Emmett–Teller (BET) measurement using a Kubo X1000. The OVs were tested without pretreatment through Electron Paramagnetic Resonance (EPR) (power: 20 db, modulation amplitude: 3, center field: 3510 G, range: 100 gauss). Volume resistance of LTO and HLTO was obtained using DC resistance measurements (Malvern Mastersizer 2000, ACL Staticide, Chicago, IL, USA) at the pressure of 3 MPa.

2.3. Electrochemical Measurement

The electrochemical performance of materials were tested using CR2032 coin-type cells (Duoduo Technology Co., Guangdong, China) assembled in an Ar-filled glove box (SG1200/750TS). The electrodes were prepared by mixing active material, Super P carbon (Aiweixin Chemical Technology Co., Shenzhen, China) black and polyvinylidene difluoride (PVDF) in a weight ratio of 8:1:1 and then hand milling with N-methyl pyrrolidone (NMP) (Tianchenghe Technology Co., Beijing, China) to obtain a homogeneous slurry. Subsequently, the slurry was coated on copper foil and dried at $80\text{ }^\circ\text{C}$ for 12 h under vacuum. The loading mass of active materials on the current collector is about $1\text{--}1.5\text{ mg cm}^{-2}$. SEM/EDX results of the LTO and HLTO electrodes (Supplementary Materials Figure S1) confirmed that both electrodes were shown with similar morphology and porosity. A pure lithium metal disc was used as the counter electrode and Celgard 2500 (Tianchenghe

Technology Co., Beijing, China) was used as the separator. The electrolyte was obtained by dissolving 1 M LiPF₆ in a mixture of ethylene carbonate (EC)/diethyl carbonate (DEC) (Duoduo Technology Co., Guangdong, China) with volume ratio of 1:1.

Galvanostatic charging–discharging profiles were tested on Neware battery tester with a voltage range of 1.0–2.5 V (vs. Li/Li⁺) at different current densities. Both cyclic voltammetry (CV) and electrochemical impedance spectroscopy (EIS) measurements were carried out on a Bio-logic SP-150 electrochemical workstation. CV was conducted with a voltage range of 1–2.5 V (vs. Li/Li⁺) at different scan rates. For EIS, both LTO and HLTO were prepared as anodes following the above-mentioned protocol, and the tests were carried out after charging at the open-circuit potential of approximately 2.7 V (voltage protection is a range from –5 V to 5 V) with a superimposed 5 mV sinusoidal (root-mean-square) perturbation over the frequency range from 0.1 to 10⁵ Hz. At least two cells were tested for each condition, which showed very similar performance. Besides, all the tests were performed using freshly assembled cells to rule out the aging effect. All cells were assembled with a configuration of an Li (counter electrode)/Celgard polymer separator/liquid electrolyte/LTO (or HLTO) anode.

2.4. Density Functional Theory (DFT) Calculations

First-principle calculations were performed via the Density Functional Theory (DFT) method coupled with the Vienna Ab-Initio Simulation Package (VASP, University of Vienna, Austria) [27]. The generalized gradient approximation (GGA) in the formulation of Perdew–Burke–Ernzerhof (PBE) was used to treat the exchange and correlation energy [28]. The cutoff energy of 450 eV was adopted for the wave basis sets. A k-points sampling with 0.04 and 0.08 Å^{−1} separation was used in the Brillouin zone for geometry optimization and density of states, respectively. The force and energy were converged to 0.02 eV Å^{−1} and 2.0 × 10^{−5} eV, respectively. The cutoff energy of 450 eV was set for the plane wave basis. The (111) plane of LTO was adopted to construct OV_s. Moreover, a 2 × 2 supercell was built in this work. The vacuum layer thickness of 20 Å was applied to avoid virtual interaction. The energy barrier was calculated using the Nudged Elastic Band (NEB) method, employing eight images between two end states. The constrained optimization of the transition state was used when the NEB method was inapplicable due to a high computational expense.

3. Results and Discussion

It is clear from Figure 1 that both the pristine and H₂-treated samples contain phase-pure Li₄Ti₅O₁₂ (JCPDS 49-0207) [29]. The bump between 20° and 30° could probably be attributed to the amorphous carbon present in the samples, which was confirmed by Raman spectroscopy (Supplementary Materials Figure S2). Typical Raman vibration bands were observed at 1348 cm^{−1} and 1588 cm^{−1}, which correspond to the D and G band of carbon. A TGA test (Supplementary Materials Figure S3) was investigated to verify such a claim. Apparently, the initial weight loss of 1.14% below 200 °C could be the evaporation of absorbed moisture content, and the subsequent loss of 2.08% between 400 and 600 °C could be due to the combustion of amorphous carbon. Furthermore, we refined XRD patterns of both samples and calculated their grain size with the Debye–Scherer formula [24,30]:

$$D = \frac{K\lambda}{B\cos\theta} \quad (1)$$

where the value of K is a constant; λ is the wavelength of X-ray; θ is the diffraction angle; B is the full-width-at-half-maximum. As a result, by calculating the D values based on the diffraction peak at 18.5° (111), the average grain size of HLTO (21.78 nm) is bigger than LTO (16.86 nm), which is most likely caused by the annealing process promoting the growth of crystallites. Moreover, the higher degree of crystallinity of HLTO (60.37%) than LTO (53.44%), which were obtained by the refinement results, also suggested the better crystallinity in the former.

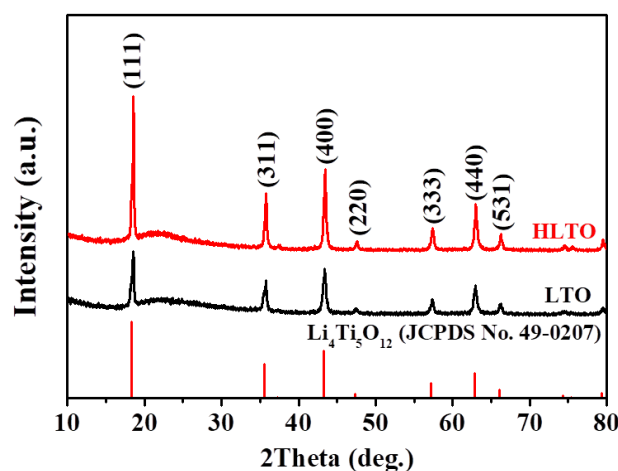


Figure 1. XRD patterns of HLTO and LTO.

On the other hand, even though both samples contained irregular submicron meter particles (Figure 2a,b), the heating process introduced subtle changes in the morphology of LTO, as HLTO seemed to have slightly larger aggregations with fewer small particles. Such a morphology was further confirmed under TEM (Figure 2c,d), and the high-resolution TEM (HRTEM) images (Figure 2e,f) showed well-defined lattice fringes with an interplanar distance of 0.48 nm, corresponding to the (111) plane of LTO in both samples. The selected-area electron diffraction (SAED) patterns display highly ordered arrangement of diffraction spots, verifying the single crystallinity of both samples. N_2 adsorption/desorption measurement was conducted to analyze the surface structure of HLTO and LTO (Supplementary Materials Figure S4). It is clear that both samples presented a typical type III isotherm [2,8] with no apparent hysteresis loop, showing a BET surface area of $10.8 \text{ m}^2 \text{ g}^{-1}$ and $13.1 \text{ m}^2 \text{ g}^{-1}$ for HLTO and LTO, respectively, and a pore size distribution with a well-defined peak at about 4 nm.

To confirm the presence of the OVs, X-ray photoelectron spectroscopy (XPS) was performed to investigate the surface chemical states of both samples (Figures 3a,b and S5). The O 1s spectra could be deconvoluted into three peaks which were located at 533.38 eV, 530.48 eV and 531.68 eV, corresponding to the hydroxyl species of surface-adsorbed water molecules, the Ti–O bonds and the OVs, respectively [8,11,20,24]. It can thus be quantified from the peak area that the content of OVs in HLTO is about 7.69%, which is about two times that of LTO (3.73%), confirming the higher concentration of OVs in the former. Ti 2p spectra for both samples (Figure 3b) showed two peaks at 459.09 eV and 464.78 eV, belonging to Ti^{4+} . The peaks at 458.08 eV and 460.88 eV correspond to Ti^{3+} , and HLTO possessed a higher Ti^{3+} level of 23.78%, while that of LTO is only 15.38%, also verifying the presence of more OVs in HLTO, suggesting that the H_2 treatment could not only introduce OVs in the material, but also effectively adjust the valence state of the Ti atoms in LTO for the overall charge balance [20,24]. The relative concentrations of OVs were further analyzed by Electron Paramagnetic Resonance (EPR) (Figure 3c). Judging by the g -values, there are two high g signals at 2.004 in HLTO and LTO, which are due to the unpaired electrons trapped by OVs, thus confirming the existence of OVs [23,29,31–33]. Meanwhile, the higher signal intensity in HLTO than LTO indicates the higher OVs concentration in the former [33–36], consistent with the above XPS analysis. Raman shift was studied to analyze the functional groups of materials and explore the influence of the OVs on Ti–O bonds (Figure 3d). Typical Raman vibration bands of LTO were observed at 227 cm^{-1} , 417 cm^{-1} and 668 cm^{-1} , which represents the bending vibration of the O–Ti–O, the stretching–bending vibrations of the Li–O bonds in LiO_4 polyhedral and the vibrations of Ti–O bonds in TiO_6 octahedra [37–39], respectively. After bringing in the OVs, the Ti–O peaks were blue-shifted, which may be caused by the asymmetric vibrations due to the replacement of Ti^{4+} by Ti^{3+} [37,38].

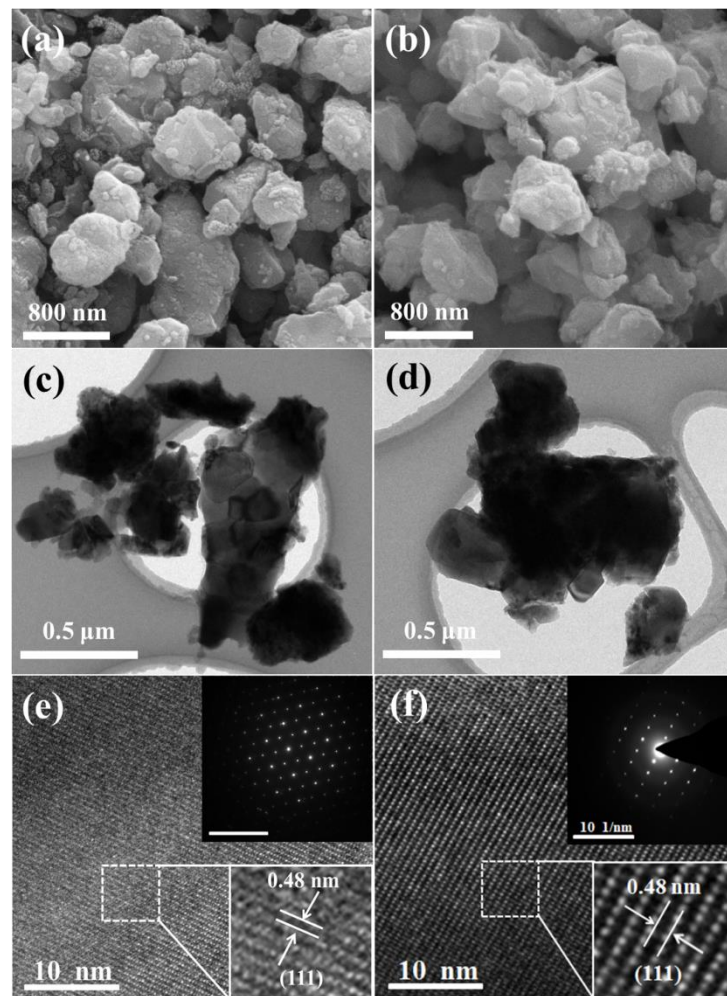


Figure 2. SEM images of (a) HLTO and (b) LTO; TEM images of (c) HLTO and (d) LTO; HRTEM images of (e) HLTO and (f) LTO. The insets in (e,f) show the SEAD patterns of the respective sample.

As illustrated in Figure 4a, both samples exhibited similar discharge capacity of 166 mAh g^{-1} and 161 mAh g^{-1} for LTO and HLTO at 1 C, respectively, and could be probably attributed to the slightly higher surface area of LTO than HLTO. Generally, such a difference is quite negligible at low current rates; however, HLTO demonstrated significantly higher capacities than LTO as the charge/discharge rate reached 5 C and beyond, further confirming the more efficient charge transfer process in the former [40,41]. Similar trend was also reflected in the cycling stability test at 1 C (Supplementary Materials Figure S6) and 5 C (Figure 4b), where a capacity advantage could be maintained in HLTO at 5 C for 300 cycles, while no noticeable difference could be observed at 1 C. The reason for this phenomenon could be that, at a low current rate, the Li^+ insertion/deinsertion and the dual-phase transformation are slow processes, the Li ions in both samples could have enough time to diffuse to the respective vacancy sites, thus producing comparable storage capacities. While testing at higher rates, the interaction between the Li ions and the active materials would be greatly limited, and only the sample with a higher Li diffusion coefficient could allow the efficient intercalation/deintercalation of Li ions within such a short reaction interval [20,24,26]. In the case of HLTO, the OV's could cause an unbalanced charge distribution in the local vicinity, which generated a built-in electric field [36,42], providing an extra driving force to the diffusion of Li^+ , giving rise to a higher specific capacity at high charge/discharge rate. A long-term stability test at 20 C (Figure 4c) presented a gradual decrease in specific capacity for 1000 cycles with almost 99.3% Coulombic efficiency, which is much higher compared to that of LTO during the

course of the test. For anodes, CE is calculated by charge capacity divided by discharge capacity, corresponding to the insertion and disinsertion of Li^+ into and from the LTO crystal framework. The initial CEs of LTO and HLTO were 99.8% and 99.6%, respectively and then stabilized at 99.1% and 99.3% after 1000 cycles at 20 C, suggesting that the insertion and deinsertion processes could take place to a similar extent. Even though both samples have similarly high CEs, HLTO delivered much higher capacities than LTO at high rates, suggesting that the diffusion of Li^+ was much more efficient in the former as more Li^+ could be inserted and deinserted during the charge/discharge process. In order for the complete storage of Li^+ , an Li metal anode was used to provide an excessive amount of Li^+ in order for both samples to uptake as much Li^+ as they can store, avoiding any possible difference in the CE values originating from the intrinsic interaction between Li^+ and LTO/HLTO, but not from the depletion of Li^+ at the electrolyte/electrode interface caused by insufficient Li^+ . Based on the above analysis, the performance and kinetic properties of HLTO were significantly improved with the introduction of OV's compared with the pristine LTO.

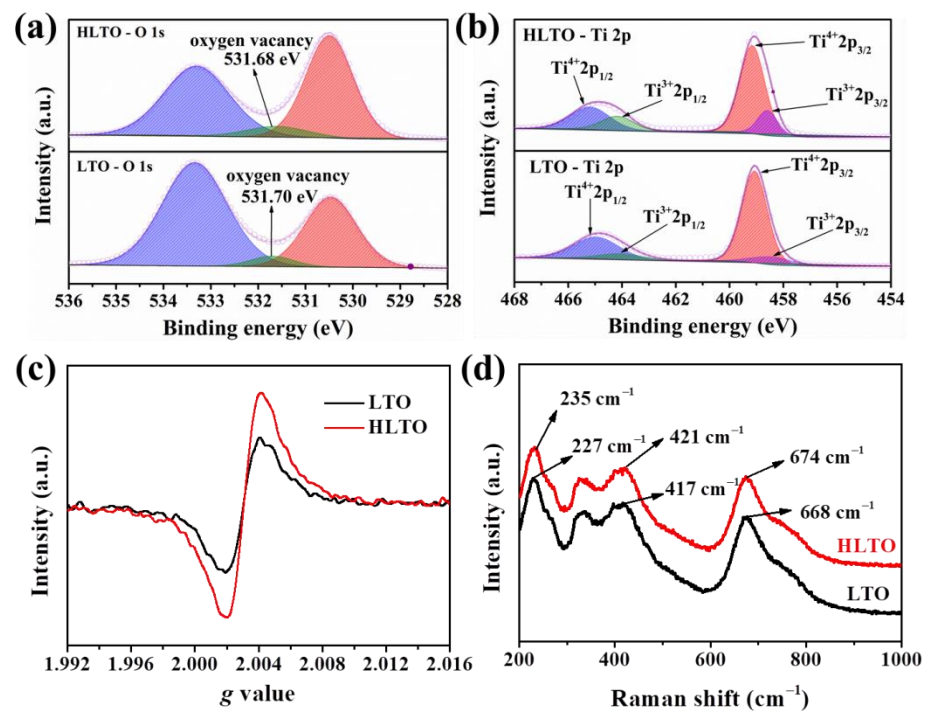


Figure 3. Characterization results of HLTO and LTO: High-resolution XPS spectra of (a) O 1s and (b) Ti 2p; (c) electron paramagnetic resonance (EPR) spectra; (d) Raman scattering spectra.

Subsequently, the galvanostatic charge/discharge curves of HLTO and LTO at various rates from 0.5 C to 30 C were investigated to inquire the capacity contributions in both samples (Figure 5a,b). It is apparent that HLTO demonstrated higher specific capacity than LTO at higher rates. Based on the analysis of the difference between the charge/discharge voltage plateaus (Supplementary Materials Figure S7), corresponding to the potential value of the distinct voltage platform from the galvanostatic charge/discharge curves, a much smaller polarization could be observed in HLTO at a high charge/discharge rate than LTO, further confirming the more efficient kinetic diffusion of Li ions. Figure 5c,d compares the discharge curves of HLTO and LTO at 1 C and 10 C, respectively. Each curve could be divided into three phases according to the potential range: the region from the open-cycle potential to ~1.55 V (noted as P1), the discharging platform at ~1.55 V (noted as P2) and a third potential region from ~1.55 V to 1 V (noted as P3) [43–45]. These three processes are related to three different reactions during discharge. P1 corresponds to the insertion of Li^+ into the LTO solid solution. The dual-phase transformation, where $\text{Li}_4\text{Ti}_5\text{O}_{12}$ transforms

into $\text{Li}_7\text{Ti}_5\text{O}_{12}$ (as shown in Equation (2) below) [46,47], is related to P2. P3 corresponds to the storage of Li^+ at solid–liquid and solid–solid interfaces.

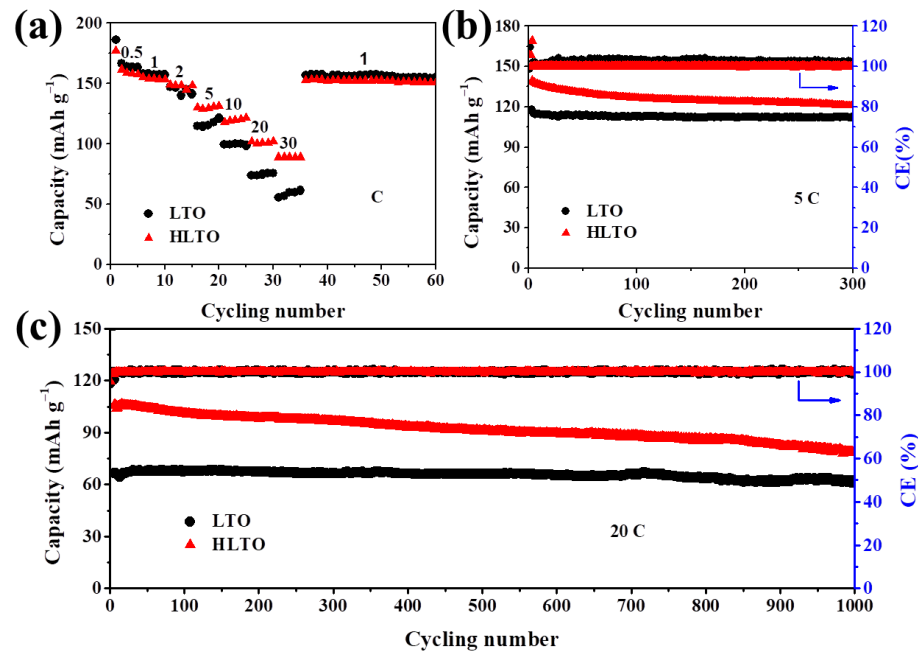
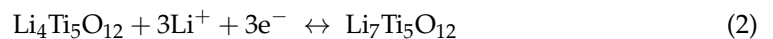


Figure 4. Electrochemical tests of LTO and HLTO: (a) Rate performance; (b) Cycling performance at 5 C; (c) Long-term cycling stability test at 20 C. All the capacities displayed in this figure are the discharge capacities.



In all cases, the P1 and P3 phases contribute only a relatively small portion of the discharge capacity, and it is also very clear that P2 played the dominant role in delivering the main capacity during discharge (Figure 5e,f). Evidently, both samples demonstrated similar capacity contributions from the three phases at the low current rate of 1 C. When the charge/discharge rate increased to 10 C, the contributions from P1 and P3 remained quite comparable, and the major difference originated from P2; that is to say, the main reason for HLTO having a higher capacity than LTO is because the former had a more efficient dual-phase transformation process than the latter [48,49].

To further study the reaction kinetics of HLTO and LTO, cyclic voltammetry (CV) analysis at different scan rates from 0.2 mV s^{-1} to 5 mV s^{-1} was conducted. The first cycles of LTO and HLTO at 0.2 mV s^{-1} are displayed in Figure 6a,c, where both samples showed a pair of well-defined redox peaks at $\sim 1.5 \text{ V}/1.65 \text{ V}$ (vs. Li/Li^+), corresponding to the Li^+ insertion/desertion of $\text{Li}_4\text{Ti}_5\text{O}_{12}$ [11–13]. It should be pointed out that HLTO demonstrated higher peak intensities compared to LTO, suggesting that the presence of OV would enhance the electrochemical processes during charge and discharge [50,51]. When increasing the scan rate to 5 mV s^{-1} , the difference in the peak intensities becomes even more prominent, suggesting a faster kinetic process in HLTO than LTO [52]. Similar to previous measurements, HLTO displayed current peaks with higher intensities than LTO at high scan rates. The relationship between the peak current (i) and the scan rate (v) could be described by an equation of $i = av^b$ [53–55], which can be transformed into:

$$\log(i) = b \log(v) + \log(a) \quad (3)$$

where b represents the charge storage behavior, and its value is usually within a range of 0.5–1. If the b is close to 0.5, the electrochemical process is mastered by ionic diffusion. On the other hand, the process is controlled by faradaic reactions when the value of

b is approaching 1 [56]. According to this theory, the b values of anodic and cathodic peaks for LTO are determined to be 0.46 and 0.36 (Figure 6b), respectively, indicating that the electrochemical process of LTO is basically controlled by ionic diffusion. In contrast, the same values of b for HLTO are 0.62 and 0.45, suggesting that there are also faradaic reactions, which could be caused by the introduced OVVs in the material [57,58].

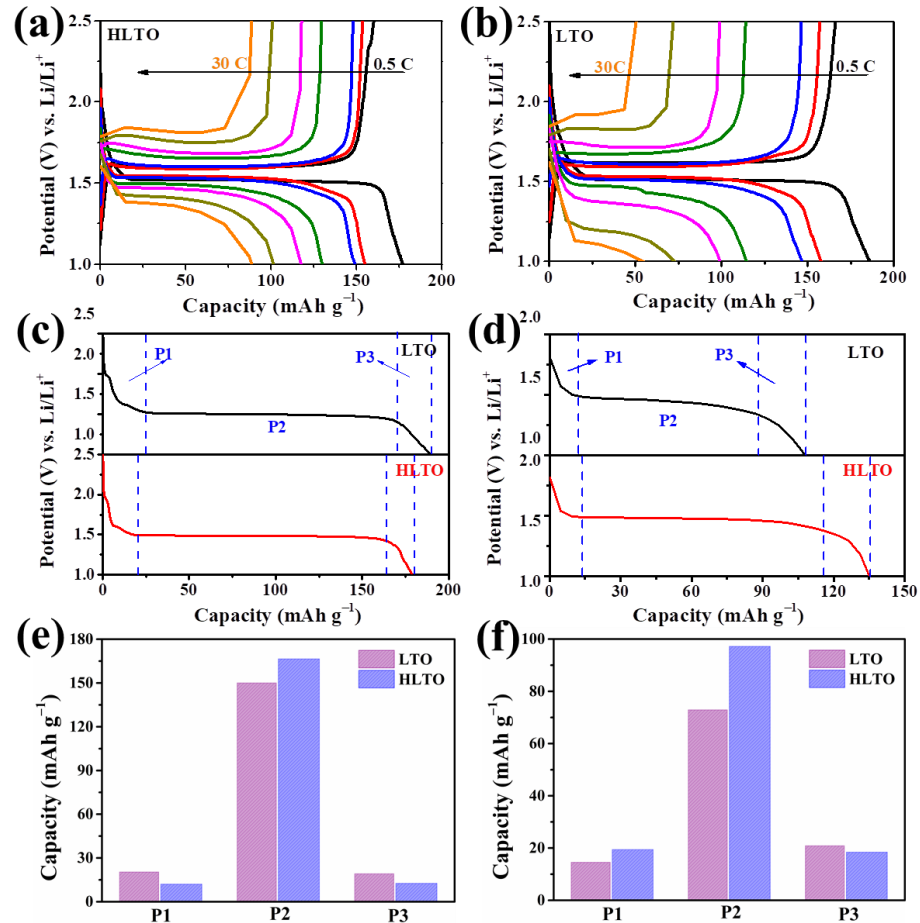


Figure 5. Charge/discharge curves of (a) HLTO and (b) LTO at various rates of 0.5 C, 1 C, 2 C, 5 C, 10 C, 20 C and 30 C; discharge curves at (c) 1 C and (d) 10 C; and the corresponding capacity contribution of different phases for HLTO and LTO at (e) 1 C and (f) 10 C.

Electrochemical impedance measurements (Figure 7) were also performed for both specimens to analyze the resistance properties. The specific frequencies at some data points have been specified (labelled in the figure). The impedance curves were fitted with the equivalent circuit model (inset of Figure 7a), where R_s represents ohmic resistance in the high frequency region and exhibits the internal resistance of electrode and electrolyte in LIBs [59], which could be obtained by the left intersection of the Nyquist plot with the Z' axis; R_{ct} refers to the charge transfer resistance at the electrolyte/LTO interface, presenting the resistance incurred on the Li ions when they inserted from the electrolyte into the LTO/HLTO crystal structure [11,60,61], which is illustrated by the semicircle in the middle frequency region; CPE corresponds to the double-layer capacitance, which could be probably attributed to the accumulation of charges on the surface of the electrode that were not inserted into the active material. Warburg impedance represents the resistance of the Li^+ ions transporting through the active material [50,62]. The diffusion coefficient of Li^+ (D_{Li^+}) through the active material LTO or HLTO could be calculated using the following equation [63,64]:

$$D_{\text{Li}^+} = \frac{R^2 T^2}{2A^2 n^4 F^4 C^2 \sigma^2} \quad (4)$$

where R is the gas constant (value is $8.314 \text{ J K}^{-1} \text{ mol}^{-1}$); T is the absolute temperature (298.15 K); A is the surface area of the electrode with a diameter of 12 mm ($1.13 \times 10^{-4} \text{ m}^2$); n is 3, which is the number of electrons transferred in the half-reaction for the redox reaction and can be acquired from Formula (2); F is the Faraday constant ($96,500 \text{ C mol}^{-1}$); C is the concentration of lithium ions ($8.3 \times 10^{-3} \text{ mol cm}^{-3}$) [64]; σ is the Warburg factor which can be acquired from the slope of $Z' \sim \omega^{1/2}$ curves, as shown in Figure 7b, and the related results for both samples are displayed in Table 1. As summarized in Table 1, HLTO exhibited a larger D_{Li^+} than LTO, which could be attributed to the improved conductivity via the introduction of OVs. Other fitting results are also listed in Table 1, and apparently, HLTO had a smaller ohmic resistance and charge transfer resistance than LTO, which was also consistent with its better high-rate performance. Besides, DC resistance measurement also showed that HLTO had a lower resistance of $5720 \Omega \cdot \text{m}$ than LTO ($16,900 \Omega \cdot \text{m}$).

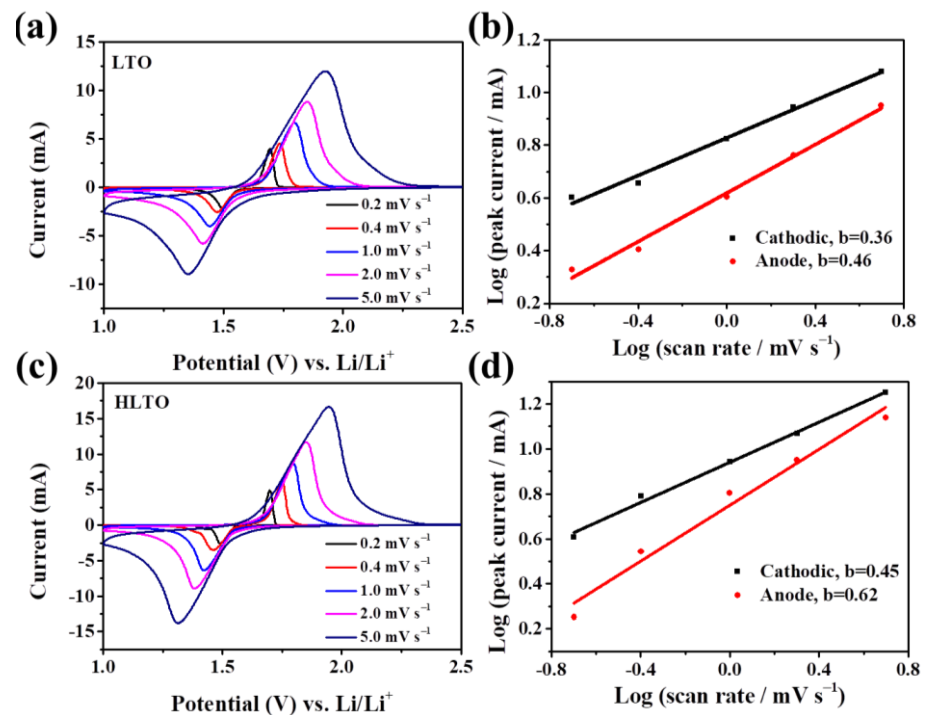


Figure 6. Kinetic analysis of the LTO and HLTO anodes: (a) CV curves at different scan rates for LTO and (b) corresponding $\log i$ versus $\log v$ plot; (c) CV curves at different scan rates for HLTO and (d) corresponding $\log i$ versus $\log v$ plot.

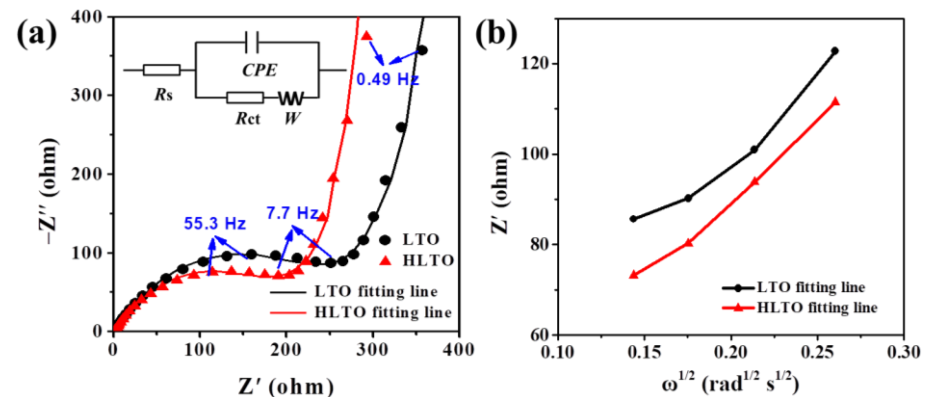


Figure 7. (a) EIS spectra of LTO and HLTO electrodes; (b) plot curves of Z' versus $\omega^{1/2}$ of three LTO electrodes in the low-frequency region. The inset in (a) shows the equivalent circuit model.

Table 1. Summary of the EIS fitting results of LTO and HLTO.

| Electrodes | R_s ($\Omega \text{ cm}^{-2}$) | R_{ct} ($\Omega \text{ cm}^{-2}$) | σ | D_{Li^+} ($\text{cm}^2 \text{ s}^{-1}$) |
|------------|------------------------------------|---------------------------------------|----------|---|
| LTO | 1.48 | 314.9 | 373.73 | 3.29×10^{-17} |
| HLTO | 0.87 | 254.3 | 297.58 | 5.18×10^{-17} |

To discover the mechanism of OV in improving the lithium storage capability, density functional theory (DFT) calculations were carried out to investigate the electronic conductivity and Li^+ diffusion behaviors in LTO lattice. Based on the XPS results, two different models of LTO with a concentration of OV of 3.9% and 7.8% were constructed, named model I and II, respectively. Considering that the coordinate numbers of Ti atoms will affect the chemical activity of LTO [65], we thus selected the (111) surface of the two models with fivefold-coordinated and fourfold-coordinated Ti atoms, corresponding to LTO with low and high OV content, respectively. The Li^+ diffusion path on the two models are displayed in Figure 8a,b, and the corresponding diffusion barriers are shown in Figure 8c. The (111) surface of LTO with high OV content (model II) exhibits a diffusion energy barrier of 0.78 eV, which is much lower than that of the sample with low OV concentration (model I; 1.62 eV), indicating that the Li^+ diffusion is faster on the surface with high OV content. This phenomenon could be attributed to the reduced interaction between Li^+ and under-coordinated Ti atoms by the OVs, thus facilitating the migration of Li^+ . The calculated density of states (DOS) of two models are shown in Figure 8d. At high OV concentration, significant changes can be observed in the DOS of LTO, giving rise to a narrowed band gap of 1.6 eV in model II. Moreover, the corresponding Fermi level exhibited an upshift from the valence band to conduction band, suggesting an enhanced electronic conductivity. These calculation results indicated that increasing oxygen vacancy concentration could enhance the electronic conductivity and lower the diffusion energy barrier of Li^+ , resulting in a fast electrochemical process and superior high-rate performance.

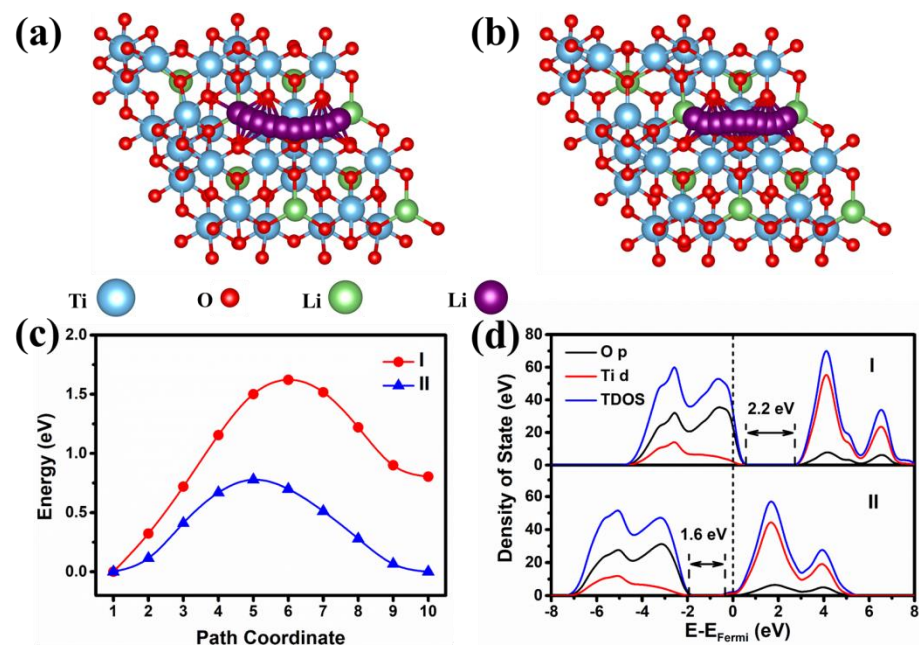


Figure 8. Li migration paths of (a) model I and (b) model II; (c) corresponding energy barriers and (d) calculated DOS of model I and model II. Model I and II correspond to the (111) surface of LTO with the OVs concentration of 3.9% and 7.8%, respectively.

4. Conclusions

In summary, by facilely treating commercial LTO under H_2 atmosphere, OVs could be efficiently introduced into the active material, giving rise to a greatly enhanced elec-

trochemical properties for lithium storage. Specifically, as confirmed by both XPS and EPR measurements, the concentration of OV_s in LTO was significantly increased after H₂ treatment, and based on density functional theory calculations, the presence of OV would enhance the electronic conductivity and lower the energy barrier of Li⁺ diffusion. As expected, HLTO with more OV_s demonstrated greatly improved high-rate performance than the pristine LTO, with a reversible capacity of 85.1 mAh g⁻¹ at a very high charge/discharge rate of 30 C, while that of LTO was only 59.9 mAh g⁻¹. For prolonged cycling at 20 C, HLTO also exhibited higher capacities than LTO. These results confirmed that this facile method of introducing OV_s into the active material would be highly effective in enhancing the high-rate performance of the electrode, shedding light on the design of high-power anode material for LIBs at an industrial scale.

Supplementary Materials: The following are available online at <https://www.mdpi.com/article/10.3390/pr9091655/s1>, Figure S1: SEM/EDX images of LTO (a), HLTO (b), Figure S2: Partial Raman spectra of HLTO and LTO, Figure S3: TGA results of commercial LTO, Figure S4: N₂ adsorption/desorption curves of HLTO and LTO. The inset shows the pore size distribution of both samples from adsorption branch, Figure S5: XPS spectra of HLTO and LTO, Figure S6: Cycling performance of LTO and HLTO at 1 C, Figure S7: The polarization results of both samples at different rates.

Author Contributions: Conceptualization, Y.Z.; Methodology, Y.Z. and X.L.; Software, S.X.; Formal Analysis, Y.Z. and Z.L.; Investigation, Y.Z., and Z.L.; Data Curation, Y.Z. and S.X.; Writing—Original Draft Preparation, Y.Z. and R.W.; Writing—Review and Editing, Y.Z. and J.C.; Supervision, J.L. and J.C. All authors have read and agreed to the published version of the manuscript.

Funding: This work was financially supported by Fundamental Research Funds for the Central Universities (ZYGX2019J030).

Institutional Review Board Statement: Not applicable.

Informed Consent Statement: Not applicable.

Data Availability Statement: Not applicable.

Conflicts of Interest: The authors declare no conflict of interest.

References

1. Gangaja, B.; Nair, S.; Santhanagopalan, D. Surface-Engineered Li₄Ti₅O₁₂ Nanostructures for High-Power Li-Ion Batteries. *Nano-Micro Lett.* **2020**, *12*, 30. [[CrossRef](#)] [[PubMed](#)]
2. He, Y.; Muhetaer, A.; Li, J.; Wang, F.; Liu, C.; Li, Q.; Xu, D. Ultrathin Li₄Ti₅O₁₂ Nanosheet Based Hierarchical Microspheres for High-Rate and Long-Cycle Life Li-Ion Batteries. *Adv. Energy Mater.* **2017**, *7*, 1700950. [[CrossRef](#)]
3. Lee, S.H.; Huang, C.; Grant, P.S. Multi-layered composite electrodes of high power Li₄Ti₅O₁₂ and high capacity SnO₂ for smart lithium ion storage. *Energy Storage Mater.* **2021**, *38*, 70–79. [[CrossRef](#)]
4. Li, Z.; Xiao, S.; Liu, J.; Niu, X.; Xiang, Y.; Li, T.; Chen, J.S. Highly Efficient Na⁺ Storage in Uniform Thorn Ball-Like α-MnSe/C Nanospheres. *Acta Metall. Sin. Engl. Lett.* **2021**, *34*, 373–382. [[CrossRef](#)]
5. Sun, J.; Guo, L.; Gao, M.; Sun, X.; Zhang, J.; Liang, L.; Liu, Y.; Hou, L.; Yuan, C. Solid-state template-free fabrication of uniform Mo₂C microflowers with lithium storage towards Li-ion batteries. *Chin. Chem. Lett.* **2020**, *31*, 1670–1673. [[CrossRef](#)]
6. Wei, C.; Fei, H.; Tian, Y.; An, Y.; Tao, Y.; Li, Y.; Feng, J. Scalable construction of SiO/wrinkled MXene composite by a simple electrostatic self-assembly strategy as anode for high-energy lithium-ion batteries. *Chin. Chem. Lett.* **2020**, *31*, 980–983. [[CrossRef](#)]
7. Zheng, H.; Zhang, H.; Fan, Y.; Ju, G.; Zhao, H.; Fang, J.; Zhang, J.; Xu, J. A novel Mo-based oxide β-SnMoO₄ as anode for lithium ion battery. *Chin. Chem. Lett.* **2020**, *31*, 210–216. [[CrossRef](#)]
8. Liu, Y.; Liu, J.; Hou, M.; Fan, L.; Wang, Y.; Xia, Y. Carbon-coated Li₄Ti₅O₁₂ nanoparticles with high electrochemical performance as anode material in sodium-ion batteries. *J. Mater. Chem. A* **2017**, *5*, 10902–10908. [[CrossRef](#)]
9. Piffet, C.; Vertruyen, B.; Caes, S.; Thomassin, J.-M.; Broze, G.; Malherbe, C.; Boschini, F.; Cloots, R.; Mahmoud, A. Aqueous processing of flexible, free-standing Li₄Ti₅O₁₂ electrodes for Li-ion batteries. *Chem. Eng. J.* **2020**, *397*, 125508. [[CrossRef](#)]
10. Qi, S.; He, J.; Liu, J.; Wang, H.; Wu, M.; Li, F.; Wu, D.; Li, X.; Ma, J. Phosphonium Bromides Regulating Solid Electrolyte Interphase Components and Optimizing Solvation Sheath Structure for Suppressing Lithium Dendrite Growth. *Adv. Funct. Mater.* **2020**, *31*, 2009013. [[CrossRef](#)]
11. Wang, D.; Liu, H.; Shan, Z.; Xia, D.; Na, R.; Liu, H.; Wang, B.; Tian, J. Nitrogen, sulfur Co-doped porous graphene boosting Li₄Ti₅O₁₂ anode performance for high-rate and long-life lithium ion batteries. *Energy Storage Mater.* **2020**, *27*, 387–395. [[CrossRef](#)]
12. Wang, H.; Wang, L.; Lin, J.; Yang, J.; Wu, F.; Li, L.; Chen, R. Structural and electrochemical characteristics of hierarchical Li₄Ti₅O₁₂ as high-rate anode material for lithium-ion batteries. *Electrochim. Acta* **2021**, *368*, 137470. [[CrossRef](#)]

13. Wang, R.; Cao, X.; Zhao, D.; Zhu, L.; Xie, L.; Li, J.; Miao, Y. Enhancing Lithium Storage Performances of the $\text{Li}_4\text{Ti}_5\text{O}_{12}$ Anode by Introducing the CuV_2O_6 Phase. *ACS Appl. Mater. Interfaces* **2020**, *12*, 39170–39180. [[CrossRef](#)] [[PubMed](#)]
14. Wen, K.; Tan, X.; Chen, T.; Chen, S.; Zhang, S. Fast Li-ion transport and uniform Li-ion flux enabled by a double-layered polymer electrolyte for high performance Li metal battery. *Energy Storage Mater.* **2020**, *32*, 55–64. [[CrossRef](#)]
15. Zhang, L.; Zhang, X.; Tian, G.; Zhang, Q.; Knapp, M.; Ehrenberg, H.; Chen, G.; Shen, Z.; Yang, G.; Gu, L.; et al. Lithium lanthanum titanate perovskite as an anode for lithium ion batteries. *Nat. Commun.* **2020**, *11*, 3490. [[CrossRef](#)]
16. Gong, S.H.; Lee, J.H.; Chun, D.W.; Bae, J.-H.; Kim, S.-C.; Yu, S.; Nahm, S.; Kim, H.-S. Effects of Cr doping on structural and electrochemical properties of $\text{Li}_4\text{Ti}_5\text{O}_{12}$ nanostructure for sodium-ion battery anode. *J. Energy. Chem.* **2021**, *59*, 465–472. [[CrossRef](#)]
17. Zhang, Q.; Verde, M.G.; Seo, J.K.; Li, X.; Meng, Y.S. Structural and electrochemical properties of Gd-doped $\text{Li}_4\text{Ti}_5\text{O}_{12}$ as anode material with improved rate capability for lithium-ion batteries. *J. Power Sources* **2015**, *280*, 355–362. [[CrossRef](#)]
18. Zhang, Q.; Zhang, C.; Li, B.; Jiang, D.; Kang, S.; Li, X.; Wang, Y. Preparation and characterization of W-doped $\text{Li}_4\text{Ti}_5\text{O}_{12}$ anode material for enhancing the high rate performance. *Electrochim. Acta* **2013**, *107*, 139–146. [[CrossRef](#)]
19. Zhao, F.; Xue, P.; Ge, H.; Li, L.; Wang, B. Na-Doped $\text{Li}_4\text{Ti}_5\text{O}_{12}$ as an Anode Material for Sodium-Ion Battery with Superior Rate and Cycling Performance. *J. Electrochem. Soc.* **2016**, *163*, A690–A695. [[CrossRef](#)]
20. Liang, K.; He, H.; Ren, Y.; Luan, J.; Wang, H.; Ren, Y.; Huang, X. Ti^{3+} self-doped $\text{Li}_4\text{Ti}_5\text{O}_{12}$ with rich oxygen vacancies for advanced lithium-ion batteries. *Ionics* **2020**, *26*, 1739–1747. [[CrossRef](#)]
21. Lyu, P.; Zhu, J.; Han, C.; Qiang, L.; Zhang, L.; Mei, B.; He, J.; Liu, X.; Bian, Z.; Li, H. Self-Driven Reactive Oxygen Species Generation via Interfacial Oxygen Vacancies on Carbon-Coated TiO_{2-x} with Versatile Applications. *ACS Appl. Mater. Interfaces* **2021**, *13*, 2033–2043. [[CrossRef](#)]
22. Shin, J.-Y.; Joo, J.H.; Samuelis, D.; Maier, J. Oxygen-Deficient $\text{TiO}_{2-\delta}$ Nanoparticles via Hydrogen Reduction for High Rate Capability Lithium Batteries. *Chem. Mater.* **2012**, *24*, 543–551. [[CrossRef](#)]
23. Xiong, T.; Yu, Z.G.; Wu, H.; Du, Y.; Xie, Q.; Chen, J.; Zhang, Y.W.; Pennycook, S.J.; Lee, W.S.V.; Xue, J. Defect Engineering of Oxygen-Deficient Manganese Oxide to Achieve High-Performing Aqueous Zinc Ion Battery. *Adv. Energy Mater.* **2019**, *9*, 1803815. [[CrossRef](#)]
24. Zhu, J.; Chen, J.; Xu, H.; Sun, S.; Xu, Y.; Zhou, M.; Gao, X.; Sun, Z. Plasma-Introduced Oxygen Defects Confined in $\text{Li}_4\text{Ti}_5\text{O}_{12}$ Nanosheets for Boosting Lithium-Ion Diffusion. *ACS Appl. Mater. Interfaces* **2019**, *11*, 17384–17392. [[CrossRef](#)]
25. Dong, C.; Dong, W.; Lin, X.; Zhao, Y.; Li, R.; Huang, F. Recent progress and perspectives of defective oxide anode materials for advanced lithium ion battery. *EnergyChem* **2020**, *2*, 100045. [[CrossRef](#)]
26. Liu, Y.; Xiao, R.; Fang, Y.; Zhang, P. Three-Dimensional Oxygen-Deficient $\text{Li}_4\text{Ti}_5\text{O}_{12}$ Nanospheres as High-Performance Anode for Lithium Ion Batteries. *Electrochim. Acta* **2016**, *211*, 1041–1047. [[CrossRef](#)]
27. Blöchl, P.E. Projector augmented-wave method. *Phys. Rev. B* **1994**, *50*, 17953–17979. [[CrossRef](#)]
28. Perdew, J.P.; Burke, K.; Ernzerhof, M. Generalized Gradient Approximation Made Simple. *Phys. Rev. Lett.* **1996**, *77*, 3865–3868. [[CrossRef](#)] [[PubMed](#)]
29. Wang, H.; Zhang, J.; Hang, X.; Zhang, X.; Xie, J.; Pan, B.; Xie, Y. Half-metallicity in single-layered manganese dioxide nanosheets by defect engineering. *Angew. Chem. Int. Edit.* **2015**, *54*, 1195–1199. [[CrossRef](#)]
30. Wang, Q.; Chen, S.; Jiang, J.; Liu, J.; Deng, J.; Ping, X.; Wei, Z. Manipulating the surface composition of Pt-Ru bimetallic nanoparticles to control the methanol oxidation reaction pathway. *Chem. Commun.* **2020**, *56*, 2419–2422. [[CrossRef](#)]
31. Wang, A.; Cao, Z.; Wang, J.; Wang, S.; Li, C.; Li, N.; Xie, L.; Xiang, Y.; Li, T.; Niu, X.; et al. Vacancy defect modulation in hot-casted NiO film for efficient inverted planar perovskite solar cells. *J. Energy. Chem.* **2020**, *48*, 426–434. [[CrossRef](#)]
32. Ye, J.; Zhai, X.; Chen, L.; Guo, W.; Gu, T.; Shi, Y.; Hou, J.; Han, F.; Liu, Y.; Fan, C.; et al. Oxygen vacancies enriched nickel cobalt based nanoflower cathodes: Mechanism and application of the enhanced energy storage. *J. Energy. Chem.* **2021**, *62*, 252–261. [[CrossRef](#)]
33. Zhang, J.; Yin, R.; Shao, Q.; Zhu, T.; Huang, X. Oxygen Vacancies in Amorphous InOx Nanoribbons Enhance CO_2 Adsorption and Activation for CO_2 Electroreduction. *Angew. Chem. Int. Edit.* **2019**, *58*, 5609–5613. [[CrossRef](#)]
34. Li, J.; Shu, C.; Liu, C.; Chen, X.; Hu, A.; Long, J. Rationalizing the Effect of Oxygen Vacancy on Oxygen Electrocatalysis in Li-O₂ Battery. *Small* **2020**, *16*, 2001812. [[CrossRef](#)] [[PubMed](#)]
35. Ni, W.; Liu, Z.; Zhang, Y.; Ma, C.; Deng, H.; Zhang, S.; Wang, S. Electroreduction of Carbon Dioxide Driven by the Intrinsic Defects in the Carbon Plane of a Single Fe-N₄ Site. *Adv. Mater.* **2021**, *33*, 2003238. [[CrossRef](#)] [[PubMed](#)]
36. Sadighi, Z.; Huang, J.; Qin, L.; Yao, S.; Cui, J.; Kim, J.-K. Positive role of oxygen vacancy in electrochemical performance of CoMn_2O_4 cathodes for Li-O₂ batteries. *J. Power Sources* **2017**, *365*, 134–147. [[CrossRef](#)]
37. Guo, M.; Chen, H.; Wang, S.; Dai, S.; Ding, L.-X.; Wang, H. TiN-coated micron-sized tantalum-doped $\text{Li}_4\text{Ti}_5\text{O}_{12}$ with enhanced anodic performance for lithium-ion batteries. *J. Alloy. Compd.* **2016**, *687*, 746–753. [[CrossRef](#)]
38. Liao, J.-Y.; Chabot, V.; Gu, M.; Wang, C.; Xiao, X.; Chen, Z. Dual phase $\text{Li}_4\text{Ti}_5\text{O}_{12}$ - TiO_2 nanowire arrays as integrated anodes for high-rate lithium-ion batteries. *Nano Energy* **2014**, *9*, 383–391. [[CrossRef](#)]
39. Tang, Y.; Huang, F.; Zhao, W.; Liu, Z.; Wan, D. Synthesis of graphene-supported $\text{Li}_4\text{Ti}_5\text{O}_{12}$ nanosheets for high rate battery application. *J. Mater. Chem.* **2012**, *22*, 11257. [[CrossRef](#)]
40. Luo, S.; Zhang, P.; Yuan, T.; Ruan, J.; Peng, C.; Pang, Y.; Sun, H.; Yang, J.; Zheng, S. Molecular self-assembly of a nanorod N- $\text{Li}_4\text{Ti}_5\text{O}_{12}$ / TiO_2 /C anode for superior lithium ion storage. *J. Mater. Chem. A* **2018**, *6*, 15755–15761. [[CrossRef](#)]

41. Qin, T.; Zhang, X.; Wang, D.; Deng, T.; Wang, H.; Liu, X.; Shi, X.; Li, Z.; Chen, H.; Meng, X.; et al. Oxygen Vacancies Boost delta-Bi₂O₃ as a High-Performance Electrode for Rechargeable Aqueous Batteries. *ACS Appl. Mater. Interfaces* **2019**, *11*, 2103–2111. [[CrossRef](#)] [[PubMed](#)]
42. Hou, C.; Hou, Y.; Fan, Y.; Zhai, Y.; Wang, Y.; Sun, Z.; Fan, R.; Dang, F.; Wang, J. Oxygen vacancy derived local build-in electric field in mesoporous hollow Co₃O₄ microspheres promotes high-performance Li-ion batteries. *J. Mater. Chem. A* **2018**, *6*, 6967–6976. [[CrossRef](#)]
43. Wang, S.; Yang, Y.; Quan, W.; Hong, Y.; Zhang, Z.; Tang, Z.; Li, J. Ti³⁺-free three-phase Li₄Ti₅O₁₂/TiO₂ for high-rate lithium ion batteries: Capacity and conductivity enhancement by phase boundaries. *Nano Energy* **2017**, *32*, 294–301. [[CrossRef](#)]
44. Xu, G.; Tian, Y.; Wei, X.; Yang, L.; Chu, P.K. Free-standing electrodes composed of carbon-coated Li₄Ti₅O₁₂ nanosheets and reduced graphene oxide for advanced sodium ion batteries. *J. Power Sources* **2017**, *337*, 180–188. [[CrossRef](#)]
45. Yang, Z.; Huang, Q.; Li, S.; Mao, J. High-temperature effect on electrochemical performance of Li₄Ti₅O₁₂ based anode material for Li-ion batteries. *J. Alloy. Compd.* **2018**, *753*, 192–202. [[CrossRef](#)]
46. Ma, J.; Wei, Y.; Gan, L.; Wang, C.; Xia, H.; Lv, W.; Li, J.; Li, B.; Yang, Q.-H.; Kang, F.; et al. Abundant grain boundaries activate highly efficient lithium ion transportation in high rate Li₄Ti₅O₁₂ compact microspheres. *J. Mater. Chem. A* **2019**, *7*, 1168–1176. [[CrossRef](#)]
47. Wu, Q.; Xu, J.; Yang, X.; Lu, F.; He, S.; Yang, J.; Fan, H.J.; Wu, M. Ultrathin Anatase TiO₂ Nanosheets Embedded with TiO₂-B Nanodomains for Lithium-Ion Storage: Capacity Enhancement by Phase Boundaries. *Adv. Energy Mater.* **2015**, *5*. [[CrossRef](#)]
48. Chen, C.; Xu, H.; Zhou, T.; Guo, Z.; Chen, L.; Yan, M.; Mai, L.; Hu, P.; Cheng, S.; Huang, Y.; et al. Integrated Intercalation-Based and Interfacial Sodium Storage in Graphene-Wrapped Porous Li₄Ti₅O₁₂ Nanofibers Composite Aerogel. *Adv. Energy Mater.* **2016**, *6*, 1600322. [[CrossRef](#)]
49. Feng, X.-Y.; Li, X.; Tang, M.; Gan, A.; Hu, Y.-Y. Enhanced rate performance of Li₄Ti₅O₁₂ anodes with bridged grain boundaries. *J. Power Sources* **2017**, *354*, 172–178. [[CrossRef](#)]
50. Huang, C.; Zhao, S.-X.; Peng, H.; Lin, Y.-H.; Nan, C.-W.; Cao, G.-Z. Hierarchical porous Li₄Ti₅O₁₂-TiO₂ composite anode materials with pseudocapacitive effect for high-rate and low-temperature applications. *J. Mater. Chem. A* **2018**, *6*, 14339–14351. [[CrossRef](#)]
51. Li, G.; Blake, G.R.; Palstra, T.T. Vacancies in functional materials for clean energy storage and harvesting: The perfect imperfection. *Chem. Soc. Rev.* **2017**, *46*, 1693–1706. [[CrossRef](#)]
52. Xu, H.; Chen, J.; Li, Y.; Guo, X.; Shen, Y.; Wang, D.; Zhang, Y.; Wang, Z. Fabrication of Li₄Ti₅O₁₂-TiO₂ Nanosheets with Structural Defects as High-Rate and Long-Life Anodes for Lithium-Ion Batteries. *Sci. Rep.* **2017**, *7*, 2960. [[CrossRef](#)] [[PubMed](#)]
53. Hong, Z.; Zhou, K.; Huang, Z.; Wei, M. Iso-Oriented Anatase TiO₂ Mesocages as a High Performance Anode Material for Sodium-Ion Storage. *Sci. Rep.* **2015**, *5*, 11960. [[CrossRef](#)] [[PubMed](#)]
54. Xiao, S.; Li, Z.; Liu, J.; Song, Y.; Li, T.; Xiang, Y.; Chen, J.S.; Yan, Q. SeC Bonding Promoting Fast and Durable Na⁺ Storage in Yolk-Shell SnSe₂@SeC. *Small* **2020**, *16*, 2002486. [[CrossRef](#)] [[PubMed](#)]
55. Xu, Y.; Zhou, M.; Zhang, C.; Wang, C.; Liang, L.; Fang, Y.; Wu, M.; Cheng, L.; Lei, Y. Oxygen vacancies: Effective strategy to boost sodium storage of amorphous electrode materials. *Nano Energy* **2017**, *38*, 304–312. [[CrossRef](#)]
56. Jiang, Y.; Song, D.; Wu, J.; Wang, Z.; Huang, S.; Xu, Y.; Chen, Z.; Zhao, B.; Zhang, J. Sandwich-like SnS₂/Graphene/SnS₂ with Expanded Interlayer Distance as High-Rate Lithium/Sodium-Ion Battery Anode Materials. *ACS Nano* **2019**, *13*, 9100–9111. [[CrossRef](#)]
57. Deng, X.; Wei, Z.; Cui, C.; Liu, Q.; Wang, C.; Ma, J. Oxygen-deficient anatase TiO₂@C nanospindles with pseudocapacitive contribution for enhancing lithium storage. *J. Mater. Chem. A* **2018**, *6*, 4013–4022. [[CrossRef](#)]
58. Kim, H.S.; Cook, J.B.; Lin, H.; Ko, J.S.; Tolbert, S.H.; Ozolins, V.; Dunn, B. Oxygen vacancies enhance pseudocapacitive charge storage properties of MoO_{3-x}. *Nat. Mater.* **2017**, *16*, 454–460. [[CrossRef](#)]
59. Yi, T.-F.; Fang, Z.-K.; Deng, L.; Wang, L.; Xie, Y.; Zhu, Y.-R.; Yao, J.-H.; Dai, C. Enhanced electrochemical performance of a novel Li₄Ti₅O₁₂ composite as anode material for lithium-ion battery in a broad voltage window. *Ceram. Int.* **2015**, *41*, 2336–2341. [[CrossRef](#)]
60. Wang, C.; Wang, S.; Tang, L.; He, Y.-B.; Gan, L.; Li, J.; Du, H.; Li, B.; Lin, Z.; Kang, F. A robust strategy for crafting monodisperse Li₄Ti₅O₁₂ nanospheres as superior rate anode for lithium ion batteries. *Nano Energy* **2016**, *21*, 133–144. [[CrossRef](#)]
61. Ge, H.; Cui, L.; Zhang, B.; Ma, T.-Y.; Song, X.-M. Ag quantum dots promoted Li₄Ti₅O₁₂/TiO₂ nanosheets with ultrahigh reversible capacity and super rate performance for power lithium-ion batteries. *J. Mater. Chem. A* **2016**, *4*, 16886–16895. [[CrossRef](#)]
62. Yuan, T.; Yu, X.; Cai, R.; Zhou, Y.; Shao, Z. Synthesis of pristine and carbon-coated Li₄Ti₅O₁₂ and their low-temperature electrochemical performance. *J. Power Sources* **2010**, *195*, 4997–5004. [[CrossRef](#)]
63. Wang, D.; Shan, Z.; Na, R.; Huang, W.; Tian, J. Solvothermal synthesis of hedgehog-like mesoporous rutile TiO₂ with improved lithium storage properties. *J. Power Sources* **2017**, *337*, 11–17. [[CrossRef](#)]
64. Wang, X.; Hao, H.; Liu, J.; Huang, T.; Yu, A. A novel method for preparation of macroporous lithium nickel manganese oxygen as cathode material for lithium ion batteries. *Electrochim. Acta* **2011**, *56*, 4065–4069. [[CrossRef](#)]
65. Wang, Y.; Sun, H.; Tan, S.; Feng, H.; Cheng, Z.; Zhao, J.; Zhao, A.; Wang, B.; Luo, Y.; Yang, J.; et al. Role of point defects on the reactivity of reconstructed anatase titanium dioxide (001) surface. *Nat. Commun.* **2013**, *4*, 2214. [[CrossRef](#)] [[PubMed](#)]